Dynamic shape transformations of fluid vesicles

Hongyan Yuan, Changjin Huang and Sulin Zhang*

Received 13th April 2010, Accepted 17th June 2010
DOI: 10.1039/c0sm00244e

We incorporate a volume-control algorithm into a recently developed one-particle-thick mesoscopic fluid membrane model to study vesicle shape transformation under osmotic conditions. Each coarse-grained particle in the model represents a cluster of lipid molecules and the inter-particle interaction potential effectively captures the dual character of fluid membranes as elastic shells with out-of-plane bending rigidity and 2D viscous fluids with in-plane viscosity. The osmotic pressure across the membrane is accounted for by an external potential, where the instantaneous volume of the vesicles is calculated *via* a local triangulation algorithm. Through coarse-grained molecular dynamics simulations, we mapped out a phase diagram of the equilibrium vesicle shapes in the space of spontaneous curvature and reduced vesicle volume. The produced equilibrium vesicle shapes agree strikingly well with previous experimental data. We further found that the vesicle shape transformation pathways depend on the volume change rate of the vesicle, which manifests the role of dynamic relaxation of internal stresses in vesicle shape transformations. Besides providing an efficient numerical tool for the study of membrane deformations, our simulations shed light on eliciting desired cellular functions *via* experimental control of membrane configurations.

Introduction

Biological membranes are two-dimensional fluids hosting a variety of lipid molecules and proteins that undergo fast lateral diffusion in physiologically relevant conditions.[1–3] They stand as truly multiscale materials: despite being only a few nanometres thick, a membrane may span up to 100 μm in the lateral dimension. In performing their biological functions, cell membranes are able to actively regulate their conformations in striking ways, exhibiting complex conformational and topological transformations. These conformational behaviors, while often contributing to the normal functions of the cell, can also initiate pathophysiological responses leading to disease.[4] Numerous phenomena indicate the intimate relationship between membrane conformations and cell functions, such as conformational changes of red blood cells infected by malaria[5] and membrane engulfment in viral budding. Understanding membrane shape transformations is thus not only fundamentally interesting, but also biologically insightful to disease diagnostics.[6,7] To separate the complex roles of membrane proteins in cell functions, artificial vesicles with different lipid compositions offer a simple model system that has been the subject of extensive studies,[8–12] of recent, particular interest is raft formation and evolution.[13–15] Amphiphilic block copolymers can also self-assemble into polymersomes of various shapes, which are proven to be much tougher and more flexible than natural membranes.[2,16] Such synthetic vesicles may find a wide range of applications such as drug delivery and encapsulation.

The high flexibility of bilayer membranes is intimately related to their small bending rigidity and their in-plane fluidity. In essence, fluid membranes carry a dual character of both a solid shell with out-of-plane bending rigidity and a 2D viscous fluid with in-plane viscosity. While such a dual character has long been recognized, how the interplay of out-of-plane curvature elasticity and in-plane viscosity determines membrane dynamics has received only limited attention.[17–20] The purpose of the present paper is to extend a recently developed mesoscopic fluid membrane model that faithfully incorporates the dual character of fluid membranes to investigate dynamic shape transformations of vesicles under prescribed osmotic conditions.

On length scales much larger than membrane thickness, bilayer membranes can be regarded as a 2D surface embedded in 3D space with its deformation behavior dictated by only a few effective mechanical properties such as bending rigidity, area compression modulus, and viscosity. Treating bilayer membranes as 2D elastic shells with zero shear resistance, elastic membrane models have been exploited in mapping out the phase diagrams of vesicle equilibrium shapes considering membrane curvature energy and the volume and area constraints.[8] The produced equilibrium membrane shapes appear to agree well with experimental observations. In these studies, the dynamics of membrane relaxation are entirely neglected. As the numerical counterpart of elastic membrane models, triangulated membrane models[19,21] successfully incorporate membrane curvature energy and account for membrane viscosity by tuning the bond-flip rate of the dynamically triangulated surface. Triangulated membrane models have been successfully applied to elucidate the critical role of membrane viscosity in suspended vesicles in simple shear flow.[18–20] A recent fluid continuum model[17] treats membranes as a 2D viscous fluid moving on a curved surface with prescribed bending rigidity and line tension, where the importance of the viscosity on the dynamic relaxation of the membranes was demonstrated.

Coarse-grained membrane simulation models, including explicit-solvent[22–24] and solvent-free models,[25–30] have been popularized in the last decade for their improved length and time scales as compared to all-atom molecular dynamics (MD)

Department of Engineering Science and Mechanics, Pennsylvania State University, University Park, PA, 16802, USA. E-mail: suz10@psu.edu

simulations and their ability to capture the dual character of fluid membranes. Coarse-grained models are attractive in simulating phase separation dynamics in multi-component membranes[31–33] and protein–membrane interactions.[34] However, treating each lipid molecule as a chain of beads, existing coarse-grained models are computationally still expensive, particularly for those with explicit solvent schemes. For this reason, studies of large-scale membrane shape transformations have still largely relied upon continuum mechanics models or the numerical methods[35–41] based on the continuum energy description.

Inspired by the pioneering work of Drouffe *et al.*,[42] many efforts have been recently devoted to develop particle-based models with high-level coarse-graining, where a bilayer membrane is represented by a monolayer or bilayer particle self-assembly.[43–46] In a recent model[46] of this type, the Drouffe model was extended to a pair potential and the bending rigidity was controlled by a time-dependent variable. Also along this line, we recently developed a one-particle-thick fluid membrane model,[47] where each particle represents a cluster of lipids in the lateral dimension. The effective membrane properties (*e.g.*, bending rigidity and area compression modulus) and the hydrophobic effect that drives the self-assembly of bilayer membranes are faithfully incorporated into an orientation-dependent pair-wise inter-particle interaction potential. The three model parameters independently and effectively control diffusion constant, bending rigidity, and spontaneous curvature, respectively. In this work, a volume-control algorithm is introduced into the fluid membrane model to study vesicle shape transformation under relevant osmotic conditions. In the present study, we neglect the hydrodynamic effect of the surrounding bulk fluid by assuming that the membrane is much more viscous than the water.

The rest of the article is organized as follows. In the following section, we briefly introduce the mesoscopic fluid membrane model. We particularly highlight the particle orientation dependence of the pair-wise inter-particle potential. Next, we propose an effective volume-control algorithm for dynamically evolving vesicles, necessary for the simulations of vesicle shape transformation due to osmotic pressure across bilayer membranes. Then, we present the shape transformation pathways of homogeneous vesicles and discuss mechanics of shape transformations. In the final section we present our conclusions.

Mesoscopic fluid membrane model

Prior to presenting our mesoscopic membrane model, it would be instructive to briefly review the energetics considerations of the elastic membrane models for comparison purposes. Treating a curved membrane as a 2D surface Ω, the bending energy can be described by the classical Helfrich–Canham curvature–elastic energy[48,49]

$$E_b = \tfrac{1}{2}\int_\Omega B(c_1 + c_2 - c_0)^2 \mathrm{d}A \quad (1)$$

where B is the bending rigidity, c_1 and c_2 are the two principal curvatures of the membrane surface, and c_0 is the spontaneous curvature. The stretching energy can be simply described by a quadratic form

$$E_s = \tfrac{1}{2}\int_\Omega K_A \varepsilon_A^2 \mathrm{d}A \quad (2)$$

where K_A is the area compression modulus, ε_A is the contour area strain. Because K_A sets a much higher energy scale than the curvature energy, bilayer membranes are generally considered as inextensible in theoretical modeling.

In our mesoscopic membrane model, an orientation-dependent inter-particle potential accounts for the two internal energies of membranes, *i.e.*, the bending energy and the area stretching energy. The potential also stabilizes the particle membrane in a fluid phase such that molecular diffusion and zero shear resistance can be naturally simulated.

Inter-particle potential

Below we briefly introduce the one-particle-thick membrane model. A detailed description of the model can be found elsewhere.[47] The mesoscopic model is solvent-free, which requires devising an effective inter-particle potential to reinstate the hydrophobic interactions between the water and lipid molecules. We found that an orientation-dependent inter-particle potential of the following form captures the hydrophobic effects most efficiently,

$$U(\mathbf{r}_{ij},\ \mathbf{n}_i, \mathbf{n}_j) = \begin{cases} u_R(r) + \left[1 - \phi(\hat{\mathbf{r}}_{ij},\ \mathbf{n}_i,\ \mathbf{n}_j)\right]\varepsilon, & r<r_{\min} \\ u_A(r)\phi(\hat{\mathbf{r}}_{ij},\ \mathbf{n}_i,\ \mathbf{n}_j), & r_{\min}<r<r_c \end{cases} \quad (3)$$

where $\boldsymbol{r}_{ij} = \boldsymbol{r}_i - \boldsymbol{r}_j$, $r = |\boldsymbol{r}_{ij}|$, $\hat{\mathbf{r}}_{ij} = \mathbf{r}_{ij}/r$, $\mathbf{r}_i$ and $\mathbf{r}_j$ are the center position vectors of particles i and j, the unit vectors $\mathbf{n}_i$ and $\mathbf{n}_j$ represent the axes of symmetry of particles i and j, respectively, as shown in Fig. 1. In addition, $r_{\min} = \sqrt[6]{2}\sigma$ sets the distance of the minimal potential energy, where σ and ε are the length and energy units, and r_c is the cutoff radius. The distance-dependent functions are

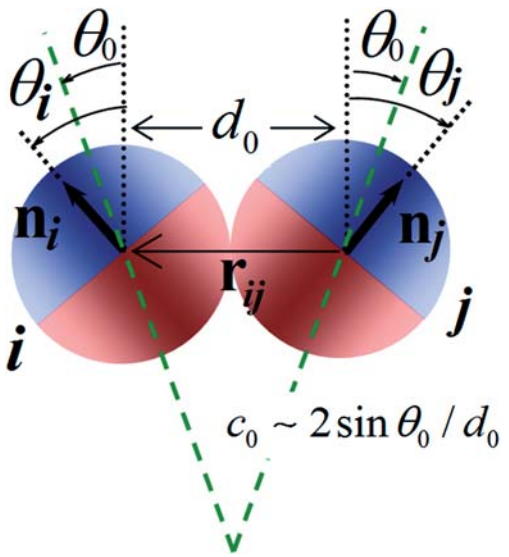

Fig. 1 Schematics of inter-particle interactions. Kinetically, each particle is axisymmetric with a particle-fixed unit vector **n** representing the axis of symmetry and a mass of m. The inter-particle interaction is both distance- and orientation-dependent. The angle θ_0 is a model parameter characterizing the spontaneous curvature. The configuration at $\theta_i = \theta_j = \theta_0$ corresponds to the energetically most favorable relative orientation between two particles. The two halves of each particle are shaded distinctly to indicate the orientation of the particle.

comprised of a soft repulsive branch $u_R(r)$ and an attractive branch $u_A(r)$:

$$u_R(r) = \varepsilon\left[\left(\frac{r_{\min}}{r}\right)^4 - 2\left(\frac{r_{\min}}{r}\right)^2\right]$$
$$u_A(r) = -\varepsilon\cos^{2\zeta}\left(\frac{\pi}{2}\frac{(r - r_{\min})}{(r_c - r_{\min})}\right) \quad (4)$$

where the parameter ζ is the exponent of the cosine function. The orientation-dependent function $\phi(\hat{\mathbf{r}}_{ij},\mathbf{n}_i,\mathbf{n}_j)$ characterizes the relative orientation between a pair of particles i and j,

$$\phi = 1 + \mu(a(\hat{\mathbf{r}}_{ij},\mathbf{n}_i,\mathbf{n}_j) - 1) \quad (5)$$

$$a = (\mathbf{n}_i \times \hat{\mathbf{r}}_{ij})\cdot(\mathbf{n}_j \times \hat{\mathbf{r}}_{ij}) + \sin\theta_0(\mathbf{n}_j - \mathbf{n}_i)\cdot\hat{\mathbf{r}}_{ij} - \sin^2\theta_0 \quad (6)$$

One notes that the function ϕ in eqn (5) linearly scales with the function a, where μ and θ_0 are two potential parameters. The functional dependence of a on its three vector variables, *i.e.*, $\hat{\mathbf{r}}_{ij}$, $\mathbf{n}_i$, $\mathbf{n}_j$, becomes clear when all the vectors are confined in a 2D plane, as shown in Fig. 1. In this simplified case, function a is reduced to

$$a = \cos\theta_i\cos\theta_j + \sin\theta_0(\sin\theta_i + \sin\theta_j) - \sin^2\theta_0 \quad (7)$$

where the definitions of θ_i, θ_j, and θ_0 can be found in Fig. 1. Assuming $\theta_i = \theta_j$ in eqn (7), a can be further simplified to $a = 1 - (\sin\theta_i - \sin\theta_0)^2$, which implies that a maximizes when $\theta = \theta_0$. The spontaneous curvature c_0 is related to θ_0 *via* $c_0 \sim 2\sin\theta_0/d_0$, where d_0 is the average inter-particle distance, as illustrated in Fig. 1. To see the functional dependence of a on θ_i and θ_j, we consider the specific case of $\theta_0 = 0°$ at which $a = \cos\theta_i\cos\theta_j$. It follows that a reaches its maximum of unity when $\mathbf{n}_i$ is parallel to $\mathbf{n}_j(\theta_i = \theta_j = 0°)$ and perpendicular to vector $\hat{\mathbf{r}}_{ij}$. The functional dependence is plotted in Fig. 2(a). The dependence of the potential U on the inter-particle distance at specified relative particle orientations is depicted in Fig. 2(b). The relative particle orientation sets the depth of the energy well of the potential, but does not affect the inter-particle distance of the minimum energy. On the other hand, the potential parameter ζ effectively tunes the slope of the attractive branch of the potential.

The simple mathematical form of the inter-particle pair potential makes it convenient to establish the correlations of the potential parameters and the membrane properties. Since ζ tunes the slope of the attractive branch of the potential and hence the restoring force dragging particles toward their equilibrium distance, it modulates the diffusivity of the particles. The parameter θ_0 specifies the spontaneous curvature, which may rise from molecular asymmetry,[49] area mismatch between two leaflets[50] of the bilayer, protein–lipid hydrophobic mismatch, or protein-assisted curvatures.[34,51] The parameter μ weighs the energy penalty when the particles are disoriented from θ_0, and is thus related to the bending rigidity of the model membrane. The area compression modulus is related to the slopes of both the attractive and repulsive branches of the potential. The independent functional dependence of the membrane properties on the potential parameters renders the model highly tunable.

Our coarse-grained molecular dynamics (CGMD) simulations showed that for μ in the range of 2.4 to 6.0 the bending rigidity ranges from $\sim 12k_BT$ to $\sim 40k_BT$ (k_BT is the thermal energy), which falls well within the range of experimental data.[47] With appropriately chosen ζ and temperature T, the particle membrane can be effectively stabilized in a fluid phase with a particle diffusion constant of $\sim 0.1\sigma^2/\tau$, where $\tau = \sigma\sqrt{m/\varepsilon}$ is the time unit. A length and time scale mapping shows that each particle represents a few lipid molecules in the lateral dimension and τ is on the order of ~ 0.1 μs.[47] Both the length and time scales of the present model are at least one order of magnitude larger than the previous solvent-free coarse-grained membrane models.[28,33] For the simulations presented in this article, the model parameters are chosen as: $\mu = 3.0$, $\zeta = 4$, $k_BT = 0.23\ \varepsilon$, which yield the membrane properties as: $B \sim 20k_BT$, $K_A \sim 18k_BT/\sigma^2$, and the particle diffusion constant of about $0.08\sigma^2/\tau$.[47] By performing a non-equilibrium molecular dynamics simulation of the Couette flow in a planar membrane, the viscosity of

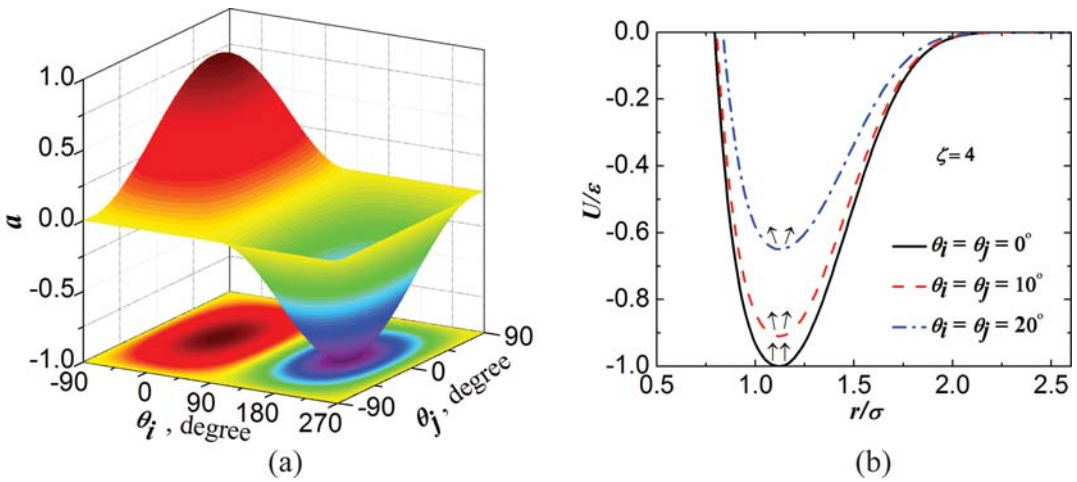

Fig. 2 Orientation dependence of the inter-particle interactions. (a) The functional dependence of a on θ_i and θ_j at $\theta_0 = 0$ shows the energetically favored and disfavored relative orientations of particles i and j. Both the 3D and 2D energy contours are plotted in the figure. Note that a larger a corresponds to a lower interaction energy. (b) The dependence of the inter-particle potential on the relative orientations of a particle pair.

the fluid membrane was found to be on the order of $1.0\varepsilon\tau/\sigma^2$ (for 2D fluid membranes, viscosity is defined as the force per unit length divided by the velocity gradient).

Equations of motion

Corresponding to the two sets of degrees of freedom, particle center positions and orientations, there are two sets of the equations of motion for the coarse-grained model. The first set governs the time evolution of the particle center positions,

$$m_i\ddot{\mathbf{r}}_i = -\frac{\partial U_i}{\partial \mathbf{r}_i} \tag{8}$$

where m_i is the mass of particle i, $U_i = \sum_j U(\mathbf{r}_{ij},\mathbf{n}_i,\mathbf{n}_j)$ and j runs over all the neighbors of i. The second set of equations governs the time evolution of the particle orientation, which can be derived from Euler's rigid body dynamics equations. However, since each particle carries only five degrees of freedom because of the geometric constraint $\mathbf{n}_i\cdot\mathbf{n}_i = 1$, the equations of motion governing particle orientations can be derived in a more efficient manner. We treat $\mathbf{n}_i$ of particle i as three generalized coordinates with the geometric constraint. Thus the governing equations for $\mathbf{n}_i$ can be derived using the Lagrange equations with constraint forces:

$$I_i\,\ddot{\mathbf{n}}_i = -\frac{\partial U_i}{\partial \mathbf{n}_i} + \lambda_i\mathbf{n}_i \tag{9}$$

where I_i is the moment of inertia ($I_i$is fixed to $1\cdot m_i\sigma^2$ in this work), λ_i is the Lagrange multiplier and has the following relation with $\mathbf{n}_i$ and $\dot{\mathbf{n}}_i$

$$\lambda_i = \frac{\partial U_i}{\partial \mathbf{n}_i}\cdot\mathbf{n}_i - I_i\,\dot{\mathbf{n}}_i\cdot\dot{\mathbf{n}}_i \tag{10}$$

Our CGMD simulations presented below for vesicles are performed in the NVT ensemble. We adopt the Nosé–Hoover thermostat[52,53] to maintain the system at desired temperatures. The rigid-body translational and rotational motions of the system are removed at each time step in our simulations, which may otherwise cause significant errors.

Vesicle volume-control algorithm

In biological processes, cells regulate their enclosed volumes by controlling the number of water molecules in the cytoplasm through the osmotic pressure difference across the membrane. We assume V_0 is the osmotically desired vesicle volume at which the osmotic pressure difference across the membrane vanishes. We denote $\hat{V}$ the volume in the absence of osmotically active molecules in solution and inside the vesicle. Therefore, $\hat{V}$ is solely determined by the membrane elasticity. The actual equilibrium volume V is a competition between osmotic potential and the membrane elastic energy. For a small deviation of the volume V from the osmotically desired volume V_0, an energy penalty arises. For simplicity, we assume that the energy penalty takes a quadratic form:

$$E_V = \frac{1}{2}K_V\left(\frac{V}{V_0}-1\right)^2 \tag{11}$$

where K_V is a constant related to the temperature, V_0, and the concentration of the osmotically active molecules.[8] In numerical simulations, K_V generally sets a higher energy scale than the bending rigidity, and thus can be regarded as a rather stiff volume spring. The hydrostatic pressure difference across the membrane, which is the negative of the osmotic pressure, is

$$p = \frac{K_V}{V_0}\left(1-\frac{V}{V_0}\right) \tag{12}$$

where positive p means outward pressure. From eqn (12), one follows that the hydrostatic pressure difference p is a function of the equilibrium vesicle volume V but usually not *vice versa* since V also depends on the membrane elasticity, as pointed out earlier.

To account for the volume constraint imposed by the enclosed water, the external potential E_V defined in eqn (11) needs to be incorporated into the total system free energy as an external potential, which requires computation of the instantaneous enclosed volume of vesicles. Calculation of the volume enclosed by a surface comprised of discrete particles necessitates triangulation or tessellation of the surface. For such a dynamically evolving particle system, triangulation poses computational challenges for the following two reasons. First, triangulation needs to be performed at each time step due to random dynamic motion of particles. An efficient triangulation algorithm is highly desired or the simulation becomes unaffordable. Second, algorithms for exact triangulation developed in computational geometry exist only for convex shapes, whereas the conformations of the vesicles under consideration may evolve into concave shapes. To circumvent these difficulties, we assume that the particles are of hexagonal close packing, and propose an approximate local triangulation algorithm as follows. For an arbitrary particle i, we identify its six nearest neighbors, forming six triangles surrounding particle i (shown in Fig. 3). Considering a triangle formed by particles i, j, and k, the triangle area A_{ijk} can be calculated using the following equation,

$$A_{ijk} = \frac{1}{2}\sqrt{(\mathbf{r}_{ji}\cdot\mathbf{r}_{ji})(\mathbf{r}_{ki}\cdot\mathbf{r}_{ki}) - (\mathbf{r}_{ji}\cdot\mathbf{r}_{ki})^2} \tag{13}$$

where $\mathbf{r}_{ji} = \mathbf{r}_j - \mathbf{r}_i$ and $\mathbf{r}_{ki} = \mathbf{r}_k - \mathbf{r}_i$, and the volume of the corresponding tetrahedron formed by the triangle and the origin O (which can be arbitrary) can be simply computed as,

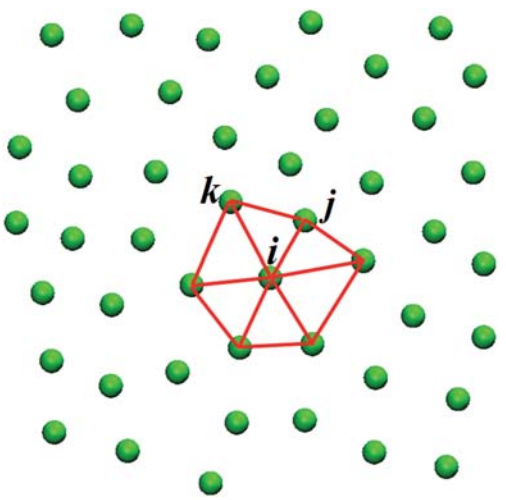

Fig. 3 Schematics of the local triangulation algorithm.

$$V_{o-ijk} = \tfrac{1}{6}\,(\mathbf{r}_j \times \mathbf{r}_k)\cdot\mathbf{r}_i \qquad (14)$$

The simple expression in eqn (14) makes it convenient to compute the forces imposed on the particles due to the volume constraint. The sequence of vectors $\mathbf{r}_j$ and $\mathbf{r}_k$ are chosen such that $\mathbf{r}_j \times \mathbf{r}_k$ points to the local outward normal of the vesicle. This is easily accomplished since the local outward normal is implied from the particle-fixed vector $\mathbf{n}_i$, but may be troublesome for other models in which the particles only carry translational degrees of freedom.

This local triangulation algorithm is robust, simple and thus efficient. Due to the random Brownian motion of the particles, the hexagonal close-packed distribution is only approximately satisfied. Nevertheless, compared to the exact triangulation (Delaunay triangulation) for a spherical vesicle, the relative error of the vesicle volume calculated by our local triangulation scheme is only about 0.2%. In the fluid membrane, the coordination number of a particle changes between five, six, and seven randomly with time. Around a particle, the local triangulation algorithm based on the six-neighbor assumption gives larger or smaller volume and area for five- or seven-neighbors, respectively. Consequently, errors of these two cases cancel each other in the global sense. This algorithm was justified by its effective volume control of the vesicles in shape transformations presented later.

Dynamics of vesicle shape transformations

Fluid vesicle configurations in equilibrium state have been extensively studied in the past several decades both experimentally and theoretically.[8,54] Among several elastic models for fluid vesicle shape determination,[8] the spontaneous curvature model searches for the equilibrium shapes of vesicles by minimizing the Helfrich–Canham curvature–elastic energy E_b given in eqn (1) under the fixed area-to-volume ratio constraint[55] and a given spontaneous curvature c_0. One notes the intimate relationship between the spontaneous curvature model and our mesoscopic model, which ensures that the present model is well suited for the simulation of vesicle shape transformations. In comparison, the bending resistance and the spontaneous curvature in our mesoscopic model are incorporated in the orientation-dependence of the potential and the potential parameter θ_0, respectively. The much larger in-plane modulus K_A sets a higher energy scale than the bending rigidity B. This in-plane and out-of-plane energy scaling ensures that the fluid membrane of the model deforms inextensibly, which fulfils the inextensibility condition imposed in the spontaneous curvature model. As an added feature, since the membrane particles are allowed to laterally diffuse and thus simulate the in-plane viscous effect, our model is capable of elucidating the rate effect of volume change on dynamics of shape transformations.

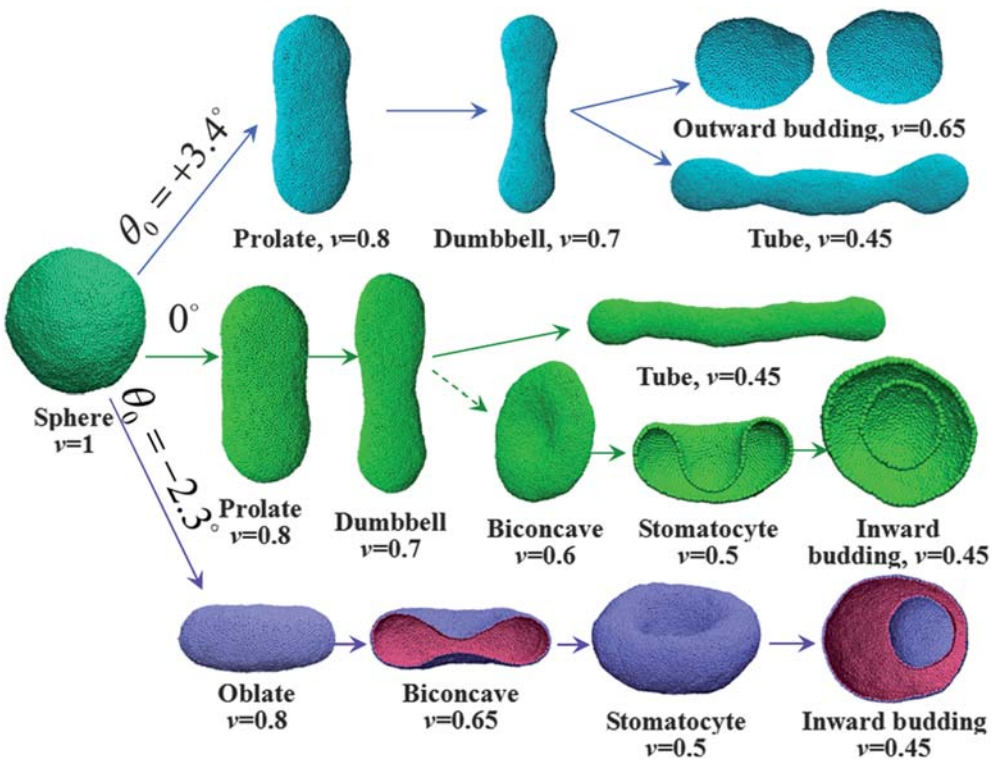

Fig. 4 Map of vesicle equilibrium shapes and shape transformation pathways. Upper pathway branch ($\theta_0 = 3.4°$): sphere, prolate, dumbbell, and outward budding (or tubular) shape for slow (or fast) volume change rate; lower pathway branch ($\theta_0 = -2.3°$): sphere, biconcave, stomatocyte, and inward budding; central pathway branch ($\theta_0 = 0°$): spherical, prolate, and dumbbell shapes, and then bifurcates into two sub-pathways. A slow volume change rate promotes dumbbell to tube shape transformation; for fast volume change rate, the vesicle follows a biconcave–stomatocyte–inward budding transformation pathway. The biconcave cannot be directly induced from the dumbbell shape, but from the spherical shape.

Equilibrium vesicle shapes and shape transformation pathways

We restrict our simulations on homogeneous vesicles, though the present model can simulate equally well the shape transformations of heterogeneous vesicles. All our simulations start with a pre-assembled, spherically shaped vesicle consisting of totally 5861 particles. We assume that the flip-flop of lipid molecules between the outer and inner leaflets of the bilayer is a rare event in the course of vesicle shape transformation, and thus prescribe a constant θ_0 to all the particles in the simulation model. Here, positive (negative) θ_0 corresponds to a convex (concave) spontaneous curvature. In experiments, osmotic pressure difference across the membrane is modulated by adding salts into the solution, effectively reducing the enclosed volume and driving the shape transformation of vesicles. We characterize the area-to-volume ratio by the reduced volume v, defined as the ratio between the volume (V) of the vesicle and the volume (V_{sphere}) of a spherical vesicle of equal area. The enclosed volume of the vesicle is then gradually reduced to the desired volume V_0 with a constant volume change rate $\dot{v}$ using the volume-control algorithm described in the previous section. Afterwards, simulation continues for a sufficiently long period until the vesicle reaches its equilibrium conformation.

Figure 4 displays the equilibrium shapes and shape transformation pathways of vesicles at three different spontaneous curvatures. We varied the volume change rate by at least an order of magnitude to explore the possible rate dependence. For a negative spontaneous curvature ($\theta_0 = -2.3°$), reducing the volume results in a shape transformation pathway consisting of a sequence of oblate, biconcave, stomatocyte shapes and inward budding. This pathway appears to be independent of the imposed volume change rates. For a positive spontaneous curvature ($\theta_0 = 3.4°$), the first two shape transformations result in prolate and dumbbell shapes. Further reducing the volume leads to shape bifurcation depending on the volume change rate. A slow volume change rate of $\dot{v} = 1.94 \times 10^{-4}\,\tau^{-1}$ induces outward budding when further reducing the volume of the vesicle from the dumbbell shape. In contrast, a high volume change rate of $\dot{v} = 1.75 \times 10^{-3}\,\tau^{-1}$ leads to dumbbell–tubular shape transformation. At zero spontaneous curvature, the vesicle shape transformation depends on the imposed volume change rate and bifurcates into two distinct pathways, each of which resembles the pathway for the cases of the positive and negative spontaneous curvatures. Independent of volume change rate, the vesicle follows prolate-to-dumbbell shape transformation for the first two steps for relatively large reduced volume ($v \geq 0.7$). For smaller reduced volume, the shape transformation bifurcates depending on the imposed volume change rate. A low volume change rate ($\dot{v} = 1.94 \times 10^{-4}\,\tau^{-1}$) promotes formation of a tubular shape. However, different from the pathways seen in the positive spontaneous curvature, the zero spontaneous curvature does not promote bifurcation from dumbbell shape to outward budding. On the other hand, the high volume change rate ($\dot{v} = 1.75 \times 10^{-3}\,\tau^{-1}$) promotes biconcave–stomatocyte–inward budding transformations. It should be pointed out that in our simulations such a transformation cannot be induced from the dumbbell shape but only directly from the spherical shape (indicated by a dashed arrow in Fig. 4). This may be due to the high energy barrier from dumbbell to biconcave shapes as compared to the thermal energy. All these equilibrium shapes and shape transformation pathways agree strikingly well with the phase diagram based on the spontaneous curvature model[55] and a recent experiment.[10] Besides yielding the shape transformation pathways, our simulation results provide insights as to how to tune the key experimental parameters quantitatively in order to induce desired shapes and shape transformations.

To understand the mechanics of vesicle shape transformation, we analyzed the dynamic evolution of the hydrostatic pressure and membrane tension. Membrane tension Σ can be calculated by the virial formula for a 2D fluid membrane that is only one-particle-thick:[47]

$$\Sigma = -\frac{3Nk_{\mathrm{B}}T}{2A} - \frac{1}{2A}\sum_{i,j>i}^{N}\mathbf{r}_{ij}\cdot\mathbf{F}_{ij} \qquad (15)$$

where A is membrane area, $\mathbf{F}_{ij}$ is the force exerted on particle i by j. Fig. 5 plots membrane tension and hydrostatic pressure at two representative spontaneous curvatures, corresponding to two shape transformation pathways: the sphere–prolate–dumbbell–tube transformation for $\theta_0 = 2.4°$ and the sphere–prolate–dumbbell–biconcave transformation for $\theta_0 = 0°$. As an overall trend, as the volume of the vesicle reduces, the hydrostatic pressure exerted on the vesicle increases. From a force-balance point of view, a negative (compressive) membrane tension is necessary to balance a negative (outer-to-inner direction) hydrostatic pressure in a convex membrane segment. Fig. 5 implies such force balance is approximately satisfied during vesicle shape transformation. It is also seen that the hydrostatic

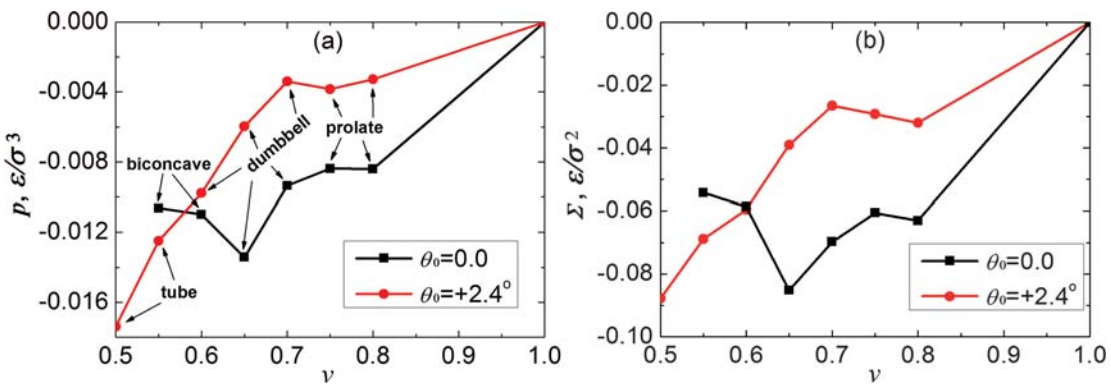

Fig. 5 Evolution of the hydrostatic pressure (a) and average membrane tension (b) with vesicle volume.

pressure abruptly decreases when the vesicle transforms from a convex to a concave conformation (*e.g.*, a dumbbell-to-biconcave transformation). The vesicle surface area was also calculated in the simulations using eqn (13), and it was found that the area change in shape transformations in the simulations is negligible.

It should be pointed out that at given hydrostatic pressure the vesicle may be stabilized at different conformations. For example, for zero spontaneous curvature at hydrostatic pressure of $\sim -0.01\varepsilon/\sigma^2$, the vesicle may adopt either a biconcave or dumbbell shape (see Fig. 5(a)). From mechanics point of view, hydrostatic pressure and volume control play roles of load-controlled and displacement-controlled loading. We adopt the latter loading mechanism since it better mimics the relevant experimental conditions.

Stress relaxation dynamics

Vesicle shape transformation is a result of strain energy relaxation of the vesicle under the prescribed enclosed volume. Considering the vesicle in our model as a viscous material, the internal stress state depends on the loading rate (the volume change rate in this case), which in turn regulates the dynamic shape transformation of the vesicles. For a low volume change rate, the vesicle has sufficient time to relax its internal stresses. On the other hand, for a relatively high volume change rate, significant stresses in the membrane could be accumulated within the vesicle. The dynamic shape transformation pathways induced by different volume change rates shown in Fig. 6 clearly manifest such a dynamic stress relaxation mechanism. For the fast volume change rate ($\dot{v} = 1.75 \times 10^{-3}\,\tau^{-1}$), the shape transformation follows a pathway sequence of spherical, triconcave, asymmetric biconcave, and biconcave shapes. Differently, a slow volume change rate ($\dot{v} = 1.94 \times 10^{-4}\,\tau^{-1}$) generates a shape transformation pathway consisting of spherical, prolate, dumbbell, and tubular shapes. It should be mentioned that, unlike the shapes presented in Fig. 4 that are dynamically equilibrated, the conformations in Fig. 6 are snapshots in the dynamic volume change processes, which are not equilibrium shapes.

To see the role of the stress relaxation in vesicle shape transformation, Fig. 7 shows the evolutions of the shear stress (a) and membrane tension (b) with changing vesicle volume. The shear

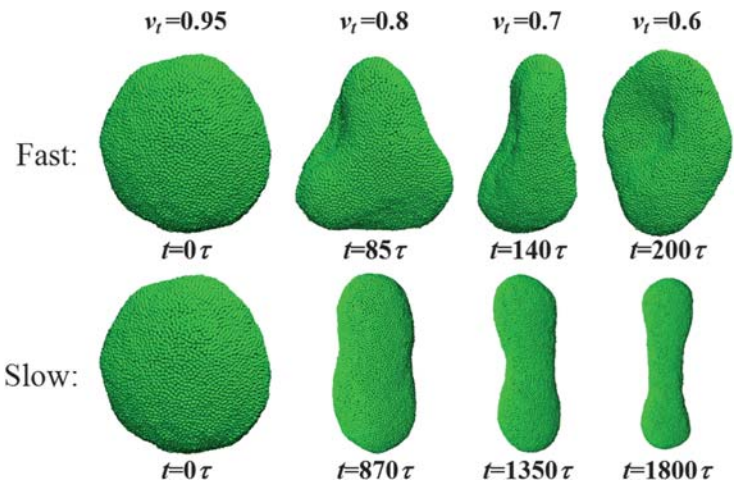

Fig. 6 Effect of the volume-change rate on the vesicle shape transformation pathways. Top panel: shape transformation pathway for fast volume-change rate ($v^{\bullet} = 1.75 \times 10^{-3}\,\tau^{-1}$); bottom panel: shape transformation pathway for low volume-change rate ($v^{\bullet} = 1.94 \times 10^{-4}\,\tau^{-1}$).

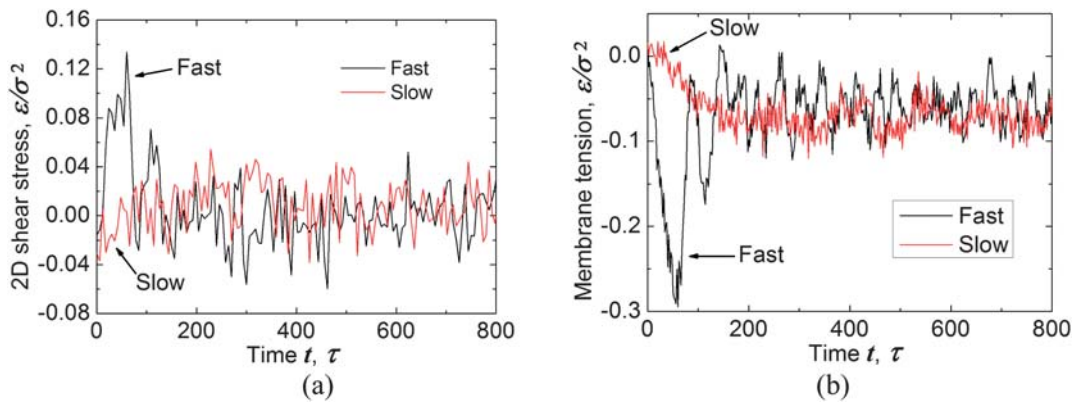

Fig. 7 Stress relaxation in dynamically evolving homogeneous vesicles at different volume-change rates. (a) Shear stress; (b) membrane tension. The reduced volume reaches 0.6 at 200 τ and 1800 τ for the fast and slow volume change rate, respectively. The shear stress is the average value of locally calculated shear stress magnitude. The curves for the shear stress in (a) are shifted vertically such that the equilibrium average value is zero. The shear stress curves in (a) look smoother than membrane tension curves in (b) because the number of data points in (a) is less than that of (b).

stress is calculated by the virial formula. For the high volume change rate, the shear stress and membrane tension undergo large undulations in the period of volume change from $v = 1.0$ to 0.6. Afterwards, the shear stress is fully relaxed to zero, while the membrane tension is relaxed to a state set by the force balance with the hydrostatic pressure. The undulations in the fully relaxed state are mainly caused by thermal fluctuations. In contrast, for the low volume change rate, both the shear stress and membrane tension undergo small undulations in the entire simulation period, indicating that the vesicle is almost fully relaxed.

Conclusions

In this article, we extend a previously established one-particle-thick fluid membrane model to study fluid vesicle shape transformations. The mesoscopic membrane model features an orientation-dependent inter-particle potential that effectively captures the dual character of lipid membranes as solid shells with out-of-plane bending rigidity and as 2D fluids with in-plane viscosity. Extension of the membrane model involves incorporating an external potential that constrains the enclosed volume of the vesicles to mimic the osmotic conditions. The extended membrane model thus enables studies of dynamics of fluid vesicle shape transformations in biologically and experimentally relevant conditions.

Shape transformation pathways of homogeneous vesicles were elaborated together with analyses of dynamic stress relaxation. The produced shape transformation pathways agree strikingly well with the experimental observations and those of previous elastic membrane models, thereby validating the simulation model. Given its great ease in modeling arbitrary vesicle conformations, the present model may be exploited to the studies of vesicle–substrate interactions,[56,57] vesicle fusions and fissions,[21,58,59] membrane–protein interactions,[21] and membrane tethering,[60] where the vesicles under investigations may adopt complex morphologies.

In contrast to elastic membrane models for which equilibrium shapes of vesicles are of the major concern, particles in our numerical model are diffusible in the lateral direction, thereby allowing the study of rate dependence of vesicle shape transformations. Our simulations showed that the shape transformation pathways can be altered by different volume-change rates, which clearly manifest the role of in-plane viscosity. The rate dependence may provide an additional controlling factor for regulating vesicle shapes and vesicle shape transformation pathways in experiments.

Acknowledgements

We acknowledge the support from National Science Foundation under Award Nos. 0826841 and 0600642.

References

1 S. J. Singer and G. L. Nicolson, *Science*, 1972, **175**, 720–731.
2 D. E. Discher and A. Eisenberg, *Science*, 2002, **297**, 967–973.
3 X. J. Li, I. V. Pivkin, H. J. Liang and G. E. Karniadakis, *Macromolecules*, 2009, **42**, 3195–3200.
4 Y. Yawata, *Cell membrane: the red blood cell as a model*, Wiley-VCH, Weinheim, Germany, 2003.
5 Y. K. Park, M. Diez-Silva, G. Popescu, G. Lykotrafitis, W. S. Choi, M. S. Feld and S. Suresh, *Proc. Natl. Acad. Sci. U. S. A.*, 2008, **105**, 13730–13735.
6 S. L. Zhang, J. Li, G. Lykotrafitis, G. Bao and S. Suresh, *Adv. Mater.*, 2009, **21**, 419–424.
7 H. Y. Yuan and S. L. Zhang, *Appl. Phys. Lett.*, 2010, **96**, 033704.
8 U. Seifert, *Adv. Phys.*, 1997, **46**, 13–137.
9 T. Baumgart, S. T. Hess and W. W. Webb, *Nature*, 2003, **425**, 821–824.
10 M. Yanagisawa, M. Imai and T. Taniguchi, *Phys. Rev. Lett.*, 2008, **100**, 148102.
11 M. Yanagisawa, M. Imai, T. Masui, S. Komura and T. Ohta, *Biophys. J.*, 2007, **92**, 115–125.
12 S. Semrau, T. Idema, T. Schmidt and C. Storm, *Biophys. J.*, 2009, **96**, 4906–4915.
13 K. Simons and W. L. C. Vaz, *Annu. Rev. Biophys. Biomol. Struct.*, 2004, **33**, 269–295.
14 M. Edidin, *Annu. Rev. Biophys. Biomol. Struct.*, 2003, **32**, 257–283.
15 T. S. Ursell, W. S. Klug and R. Phillips, *Proc. Natl. Acad. Sci. U. S. A.*, 2009, **106**, 13301–13306.
16 G. Srinivas, D. E. Discher and M. L. Klein, *Nat. Mater.*, 2004, **3**, 638–644.
17 M. Arroyo and A. DeSimone, *Phys. Rev. E: Stat., Nonlinear, Soft Matter Phys.*, 2009, **79**, 031915.
18 H. Noguchi and G. Gompper, *Phys. Rev. Lett.*, 2004, **93**, 258102.
19 H. Noguchi and G. Gompper, *Proc. Natl. Acad. Sci. U. S. A.*, 2005, **102**, 14159–14164.
20 H. Noguchi and G. Gompper, *Phys. Rev. E: Stat., Nonlinear, Soft Matter Phys.*, 2005, **72**, 011901.
21 E. Atilgan and S. X. Sun, *J. Chem. Phys.*, 2007, **126**, 095102.
22 R. Goetz and R. Lipowsky, *J. Chem. Phys.*, 1998, **108**, 7397–7409.
23 R. Goetz, G. Gompper and R. Lipowsky, *Phys. Rev. Lett.*, 1999, **82**, 221–224.
24 S. J. Marrink, H. J. Risselada, S. Yefimov, D. P. Tieleman and A. H. de Vries, *J. Phys. Chem. B*, 2007, **111**, 7812–7824.
25 H. Noguchi and M. Takasu, *Phys. Rev. E: Stat., Nonlinear, Soft Matter Phys.*, 2001, **64**, 041913.
26 O. Farago, *J. Chem. Phys.*, 2003, **119**, 596–605.
27 Z. J. Wang and D. Frenkel, *J. Chem. Phys.*, 2005, **122**, 234711.
28 I. R. Cooke and M. Deserno, *J. Chem. Phys.*, 2005, **123**, 224710.
29 G. Brannigan, P. F. Philips and F. L. H. Brown, *Phys. Rev. E: Stat., Nonlinear, Soft Matter Phys.*, 2005, **72**, 011915.
30 G. S. Ayton and G. A. Voth, *J. Phys. Chem. B*, 2009, **113**, 4413–4424.
31 M. Laradji and P. B. Kumar, *Phys. Rev. E: Stat., Nonlinear, Soft Matter Phys.*, 2006, **73**, 040901.
32 M. Laradji and P. B. Sunil Kumar, *Phys. Rev. Lett.*, 2004, **93**, 198105.
33 I. R. Cooke, K. Kremer and M. Deserno, *Phys. Rev. E: Stat., Nonlinear, Soft Matter Phys.*, 2005, **72**, 011506.
34 B. J. Reynwar, G. Illya, V. A. Harmandaris, M. M. Muller, K. Kremer and M. Deserno, *Nature*, 2007, **447**, 461–464.
35 J. Li, M. Dao, C. T. Lim and S. Suresh, *Biophys. J.*, 2005, **88**, 3707–3719.
36 M. Dao, J. Li and S. Suresh, *Mater. Sci. Eng. C-Biomimetic Supramol. Syst.*, 2006, **26**, 1232–1244.
37 J. Li, G. Lykotrafitis, M. Dao and S. Suresh, *Proc. Natl. Acad. Sci. U. S. A.*, 2007, **104**, 4937–4942.
38 F. Feng and W. S. Klug, *J. Comput. Phys.*, 2006, **220**, 394–408.
39 L. T. Gao, X. Q. Feng and H. J. Gao, *J. Comput. Phys.*, 2009, **228**, 4162–4181.
40 T. Biben, K. Kassner and C. Misbah, *Phys. Rev. E: Stat., Nonlinear, Soft Matter Phys.*, 2005, **72**, 041921.
41 Q. Du, C. Liu and X. Q. Wang, *J. Comput. Phys.*, 2004, **198**, 450–468.
42 J. M. Drouffe, A. C. Maggs and S. Leibler, *Science*, 1991, **254**, 1353–1356.
43 G. Brannigan and F. L. H. Brown, *J. Chem. Phys.*, 2004, **120**, 1059–1071.
44 H. Noguchi and G. Gompper, *Phys. Rev. E: Stat., Nonlinear, Soft Matter Phys.*, 2006, **73**, 021903.
45 P. Ballone and M. G. Del Popolo, *Phys. Rev. E: Stat., Nonlinear, Soft Matter Phys.*, 2006, **73**, 031404.
46 T. Kohyama, *Phys. A*, 2009, **388**, 3334–3344.
47 H. Yuan, C. Huang, J. Li, G. Lykotrafitis and S. Zhang, *Physical Review E*, 2010, **82**, 011905.
48 P. B. Canham, *J. Theor. Biol.*, 1970, **26**, 61–81.
49 W. Helfrich, *Z. Naturforsch., C: J. Biosci.*, 1973, **C 28**, 693–703.

50 M. P. Sheetz and S. J. Singer, *Proc. Natl. Acad. Sci. U. S. A.*, 1974, **71**, 4457–4461.
51 P. D. Blood and G. A. Voth, *Proc. Natl. Acad. Sci. U. S. A.*, 2006, **103**, 15068–15072.
52 S. Nosé, *Mol. Phys.*, 1984, **52**, 255–268.
53 W. G. Hoover, *Phys. Rev. A: At., Mol., Opt. Phys.*, 1985, **31**, 1695–1697.
54 J. Kas and E. Sackmann, *Biophys. J.*, 1991, **60**, 825–844.
55 U. Seifert, K. Berndl and R. Lipowsky, *Phys. Rev. A: At., Mol., Opt. Phys.*, 1991, **44**, 1182–1202.
56 J. O. Rädler, T. J. Feder, H. H. Strey and E. Sackmann, *Phys. Rev. E: Stat. Phys., Plasmas, Fluids, Relat. Interdiscip. Top.*, 1995, **51**, 4526–4536.
57 A. Albersdorfer, T. Feder and E. Sackmann, *Biophys. J.*, 1997, **73**, 245–257.
58 H. Noguchi and M. Takasu, *J. Chem. Phys.*, 2001, **115**, 9547–9551.
59 J. C. Shillcock and R. Lipowsky, *J. Phys.: Condens. Matter*, 2006, **18**, S1191–S1219.
60 D. Cuvelier, I. Derenyi, P. Bassereau and P. Nassoy, *Biophys. J.*, 2005, **88**, 2714–2726.